

Pseudo Point Nodal Superconducting Gap in Spin-Triplet UTe₂

S. Hosoi^{1,*}, K. Imamura^{1,2}, M.M. Bordelon¹, E.D. Bauer¹, S.M. Thomas¹,
F. Ronning¹, P.F.S. Rosa¹, R. Movshovich¹, I. Vekhter³, and Y. Matsuda^{1,†}

¹*Los Alamos National Laboratory, Los Alamos, NM 87545, USA*

²*Department of Advanced Materials Science, University of Tokyo, Chiba 277-8561, Japan and*

³*Department of Physics and Astronomy, Louisiana State University, Baton Rouge, LA 70803-4001, USA*

The unconventional superconductor UTe₂ represents a rare example of spin-triplet pairing with potentially topologically protected quantum states. However, conflicting reports on its gap structure—particularly regarding point nodes—have hindered understanding of the order parameter symmetry and topological properties. Here, we report high-resolution thermal conductivity measurements on high-quality UTe₂ single crystals down to ~ 50 mK that definitively resolve the gap anisotropy through bulk directional transport. The b -axis thermal conductivity κ_b/T exhibits negligible residual conductivity at $T \rightarrow 0$ and its temperature dependence is consistent with a small superconducting energy gap along the b -axis. Under magnetic fields, the residual κ_b/T exhibits weak field-induced enhancement. Remarkably, a threshold field emerges at low fields for $H \parallel a$, characterized by a kink that signals a change in the quasiparticle transport normal to the field. Below the threshold, κ_b/T remains isotropic for all field orientations, whereas strong anisotropy between transport along and normal to the field develops above it. These signatures strongly suggest that UTe₂ exhibits a fully gapped state with a pseudo point-nodal structure—where gap minima approach but never reach zero. We estimate the minimal gap $\Delta_{\min}/\Delta_0 \sim 0.1$ along the b -axis, where Δ_0 is the characteristic superconducting gap. This highly unusual gap structure provides crucial insights into the exotic pairing mechanisms and topology of this spin-triplet superconductor, excluding non-unitary mixing of pairing symmetries.

Spin-triplet superconducting states have garnered significant attention due to their unconventional pairing mechanism and potential to host topologically protected Majorana zero modes, which offer a promising platform for fault-tolerant topological quantum computation [1]. While liquid ³He exemplifies spin-triplet superfluidity, identifying solid-state analogs remains a central challenge in condensed matter physics. Recently, the heavy fermion superconductor UTe₂ has emerged as an ex-

ceptionally promising candidate for realizing spin-triplet superconductivity [2]. This uranium-based compound exhibits a constellation of anomalous superconducting properties that collectively provide compelling evidence for unconventional pairing mechanisms. Most notably, UTe₂ displays extraordinarily large upper critical fields H_{c2} that substantially exceed the Pauli paramagnetic limit [2, 3]. The superconducting phase diagram under both magnetic field and pressure reveals additional complexity through the existence of multiple distinct superconducting phases [4–8], indicating highly unusual pairing states.

Critically, the unconventional superconducting state in UTe₂ emerges from a paramagnetic normal state at ambient pressure, distinguishing it from uranium-based compounds such as UGe₂ [9], URhGe [10], and UCoGe [11], where superconductivity coexists with ferromagnetic order. Moreover, the Fermi surface structure of UTe₂ appears to be simpler than that of many other heavy fermion superconductors, with fewer sheets and less complex topology [3, 12–14]. These characteristics establish UTe₂ as an ideal model system for investigating spin-triplet superconductivity.

The comprehensive characterization of the superconducting gap structure in UTe₂ represents a critical prerequisite for understanding the Cooper pair formation mechanism and determining its topological nature. However, despite extensive experimental investigations, the precise gap structure of UTe₂ remains unresolved. The challenge is further amplified by pronounced surface-bulk electronic structure disparities, most notably manifested through the emergence of a surface charge density wave (CDW) instability that does not occur in the bulk [15–17]. The surface-bulk dichotomy presents systematic challenges for interpreting surface-sensitive spectroscopic techniques, including scanning tunneling microscopy (STM) [18] and tunnel junction measurements [19, 20]. Additionally, magnetic penetration depth measurements [21–23] may be influenced by the sample edge [23] or anomalous surface normal state [22]. We also note that, since low-energy quasiparticle excitations in UTe₂ are particularly sensitive to disorder, ultraclean crystals are required, whereas lower quality samples obscure intrinsic gap features.

Thermodynamic measurements under uniaxial strain [24] and ultrasound measurement [25], combined with polar Kerr effect spectroscopy [26] and muon spin relax-

corresponding authors:

*shosoi@lanl.gov, †matsuda@lanl.gov

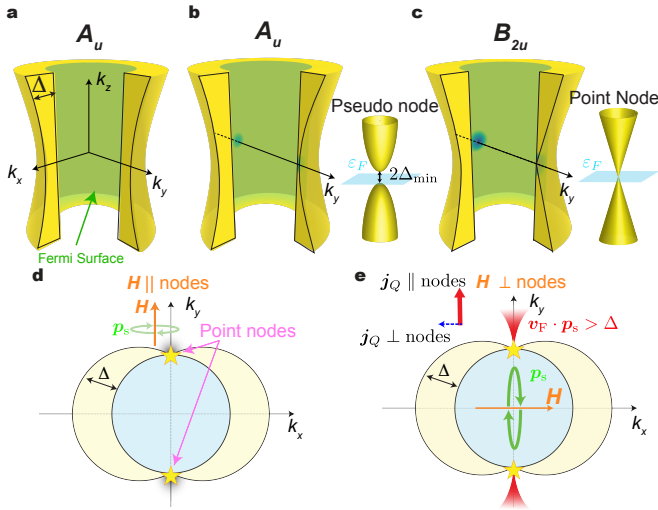


FIG. 1. Superconducting gap structure and Doppler shift: **a, b, c:** Superconducting gap structure Δ (yellow) on a 2D cylindrical Fermi surface (yellow-green) for A_u (**a** and **b**) and B_{2u} (**c**) symmetries. **a:** Full gap opens uniformly. **b:** At pseudo point nodes, the gap amplitude approaches zero but remains finite. The accompanying figure (right) shows the quasiparticle dispersion in the vicinity of the gap minimum. **c:** The B_{2u} state hosts point nodes (dark green) along the b -axis (k_y direction). The Dirac cone emerges where the gap amplitude vanishes at a point node. **d,e:** Schematic representation of Doppler shift effects under magnetic field H applied perpendicular and parallel to point nodes, respectively. The supercurrent velocity v_s circulating around vortex cores is oriented perpendicular to H . **d:** For $H \parallel$ nodes, Doppler-shifted quasiparticle excitations are suppressed due to $v_F \cdot p_s = 0$. **e:** For $H \perp$ nodes, the Doppler shift energy $v_s \cdot p_s$ exceeds the superconducting gap magnitude Δ , thereby activating low-energy quasiparticle excitations in the nodal directions (red-shaded region). When thermal current j_Q is applied parallel to the nodal directions ($j_Q \parallel$ nodes), thermal conductivity exhibits selective sensitivity to nodal excitations, while it becomes insensitive when $j_Q \perp$ nodes.

ation measurements [27], have provided evidence against bulk chiral superconductivity. Accordingly, four single-component irreducible representations within the D_{2h} point group characterize potential spin-triplet pairing states: A_u (fully gapped, Figs. 1a and 1b), B_{1u} (point nodes along the crystallographic c -axis), B_{2u} (point nodes along the b -axis, Fig. 1c), and B_{3u} (point nodes along the a -axis).

A definitive determination of the superconducting order parameter requires directionally-resolved, bulk-sensitive experimental probes capable of directly accessing nodal quasiparticle excitations at ultra-low temperatures [28]. In contrast to specific heat, thermal conductivity preferentially samples itinerant quasiparticles with the Fermi velocity v_F parallel to the thermal current j_Q . Since in anisotropic superconductors at low energies such quasiparticles are confined to the regions when the gap is minimal, the directional dependence of thermal transport reflects the underlying nodal structure. Notably, thermal

conductivity remains immune to extrinsic Schottky contributions, permitting measurements at sufficiently low temperatures to unambiguously differentiate nodal and gapped states. Most significantly, as the magnetic field also serves as a directional probe that excites quasiparticles through the Doppler shift of the quasiparticle spectra, the combination of magnetic field orientation with thermal conductivity measurements constitutes a powerful probe for superconducting gap determination, enabling precise mapping of nodal directions (Figs. 1d and 1e).

Thermal conductivity studies in UTe_2 have established the absence of point nodes along the a direction through the a -axis thermal conductivity (κ_a) measurements ($j_Q \parallel a$) [29, 30]. In contrast, the conclusions regarding point nodes along the b axis remain controversial. This discrepancy arises because κ_a measurements probe mostly the quasiparticles with the Fermi velocity along the a -axis, and are much less sensitive to the excitations in the vicinity of the potential b -axis nodes (Fig. 1e). While b -axis thermal conductivity (κ_b) measurements ($j_Q \parallel b$) would directly probe the b -axis nodal structure, such experiments were previously precluded by insufficient sample sizes along the b direction, preventing definitive determination of the complete nodal topology.

Here, we measured the thermal conductivity κ_b along the b -axis using molten-salt-grown ultraclean single crystals [31] (lower inset of Fig. 2a). The upper inset of Fig. 2a shows the resistivity along the b -axis, ρ_b , plotted as a function of T^2 for samples #A and #B. The resistivity follows standard Fermi-liquid behavior, described by $\rho_b(T) = \rho_b^0 + AT^2$. This behavior is consistently observed under magnetic field $H \parallel a$ down to very low temperatures (Supplementary Fig. 1). We estimated residual resistivities of $\rho_b^0 \approx 1.72 \mu\Omega\text{cm}$ for sample #A and $\approx 2.12 \mu\Omega\text{cm}$ for sample #B in zero field. These values correspond to residual resistivity ratios of $RRR \equiv \rho_b(300\text{K})/\rho_b^0 \approx 410$ and ≈ 350 for samples #A and #B, respectively.

We first examine the zero-field thermal conductivity. We confirmed the Wiedemann-Franz law, providing stringent validation of thermal conductivity measurement accuracy (Supplementary Fig. 2). The main panel of Fig. 2a depicts the temperature dependence of κ_b . At the superconducting transition temperature $T_c = 2.1\text{K}$, κ_b/T exhibits a pronounced discontinuity, followed by a pronounced maximum at around 1.2K. The enhancement below T_c for #B (with lower RRR) is slightly suppressed compared to #A. This enhancement arises from the dramatic increase in quasiparticle mean free path, which results from suppressed electron-electron inelastic scattering following superconducting gap opening.

The temperature dependence of κ_b/T at very low temperatures for both sample #A and #B is shown in Fig. 2b. Similar to κ_a/T [29, 30], κ_b/T decreases monotonically upon cooling. As shown in the inset of Fig. 2b, κ_b/T exhibits a nearly T^2 dependence. The thermal conductivity in the superconducting state comprises quasipar-

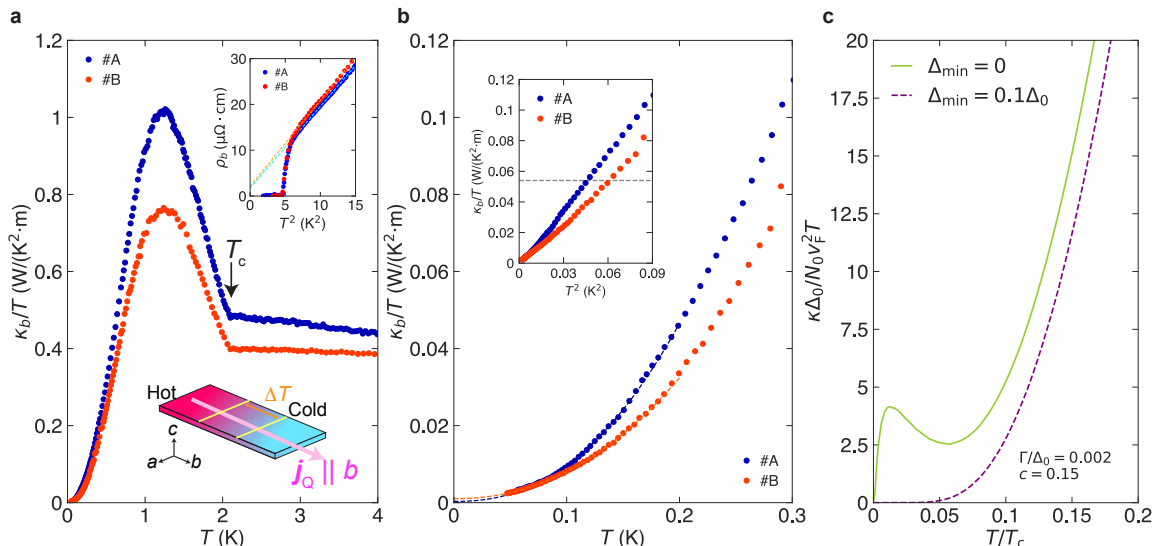


FIG. 2. **Thermal conductivity in zero magnetic field:** **a**, The main panel shows the b -axis thermal conductivity divided by temperature, κ_b/T , in zero field for sample #A ($RRR \approx 410$) and #B ($RRR \approx 350$). Both samples exhibit a sharp discontinuity at T_c (arrow). The lower inset illustrates the experimental configuration for thermal conductivity measurements with thermal current \mathbf{j}_Q applied along the crystallographic b -axis. The upper inset shows electrical resistivity along the b -axis in zero field plotted as a function of T^2 for #A and #B. $\rho_b(T)$ is well fit by $\rho_b(T) = \rho_b^0 + AT^2$ (orange and cyan dashed line, respectively). **b**, κ_b/T in zero field for #A and #B at very low temperatures. The inset shows κ_b/T vs. T^2 . The gray dashed line indicates the residual thermal conductivity expected for a superconductor with line nodes in the gap structure. **c**, Calculated temperature dependence of κ/T for point nodes ($\Delta_{\min} = 0$) and pseudo point nodes ($\Delta_{\min} = 0.1\Delta_0$), with heat current parallel to the nodal direction.

ticle and phonon contributions. As discussed below, our results strongly indicate a substantial quasiparticle component in the measured thermal conductivity at low temperatures. For superconductors with line nodes, the low temperature residual thermal conductivity has a universal, impurity-independent, slope, which for UTe_2 is estimated to be $\kappa_{00}/T \approx 0.054 \text{ W/K}^2\text{m}$ (gray dashed line in the inset of Fig. 2b) [29]. The extrapolation of κ_b/T to zero temperature (red and blue dotted lines in the main panel of Fig. 2b) yields a vanishing intercept within experimental accuracy, indicating negligibly small residual thermal conductivity, with an upper bound estimate of $\kappa_b^0/T = 0.0017 \text{ W/K}^2\text{m}$ for both #A and #B. Thus κ_b^0/T is significantly smaller than κ_{00}/T , similar to κ_a/T [29, 30]. These results exclude line-nodal gap structures compatible with D_{2h} symmetry under weak spin-orbit coupling, constraining the pairing to either a full gap or point nodes as expected in the strong spin-orbit coupling regime.

Temperature dependence of κ_b/T in zero field provides pivotal information regarding the presence or absence of point nodes along the b -axis [30]. For the heat current along the point nodes, the residual term in the thermal conductivity is finite only if the impurity scattering rate, Γ , exceeds a threshold value, and vanishes otherwise [32]. The threshold value is finite for any scattering phase shift, δ , away from the unitary limit ($c = \cot \delta = 0$). Therefore, the near absence of the residual linear term observed here is strongly suggestive of a clean sample

($\Gamma \ll \Delta_0$) with a finite c , although it may be also consistent with a sample of extreme purity in the unitary limit. For all clean samples with a finite c and the heat current along a point node a key feature of the temperature dependence of κ/T is the non-monotonicity, the emergence of a characteristic peak at low temperature [32, 33]. This peak disappears if a small gap opens in the nodal region.

Figure 2c shows the calculated κ/T (normalized as $\kappa\Delta_0/N_0v_F^2T$, where N_0 is the normal-state density of states, and v_F is the Fermi velocity) as a function of T/T_c for true point nodes ($\Delta_{\min} = 0$) and pseudo point nodes ($\Delta_{\min} = 0.1\Delta_0$), with \mathbf{j}_Q applied parallel to the nodal direction. Here, we use representative values $\Gamma/\Delta_0 = 0.002$ and $c = 0.15$. Technical details of the calculations and additional data demonstrating that this is a generic behavior are given in the Supplementary Information. Our samples exhibit negligibly small residual thermal conductivity. In the presence of point nodes along the b -axis, a low-temperature peak in κ_b/T would be expected. Given that the quasiparticle contribution dominates the thermal conductivity, such a peak would be experimentally detectable. However, no indication of a peak is observed in either κ_b/T or κ_a/T [29, 30], strongly suggesting a nodeless superconducting gap structure in the ab -plane.

Thermal conductivity measurements with applied magnetic fields along three crystallographic orientations provide a more stringent and direct test for the absence of point nodes and the presence of a small gap. Magnetic fields induce circulating supercurrents around vor-

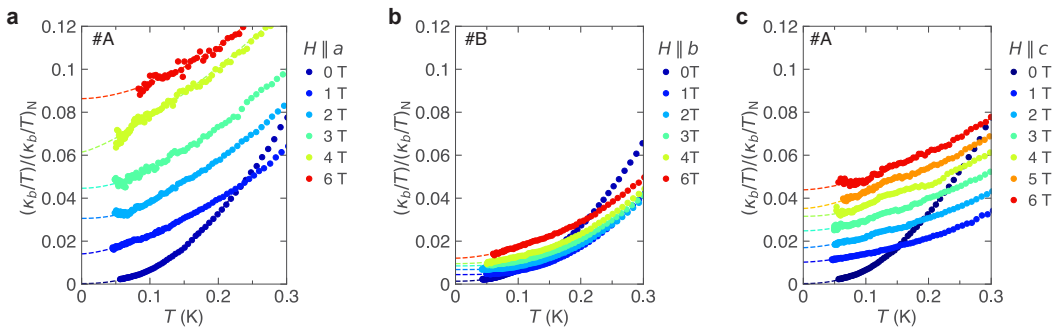


FIG. 3. **Low temperature thermal conductivity under magnetic fields along each crystallographic axis: a,b,c**, Temperature dependence of low-temperature thermal conductivity along the b -axis under magnetic fields applied parallel to the a -axis (a), b -axis (b), and c -axis (c), respectively. The dashed lines represent polynomial fitting results.

tices characterized by the superfluid momentum $\mathbf{p}_s(\mathbf{r})$ in the plane normal to the field. The resulting Doppler shift in quasiparticle energy, $E_k \rightarrow E_k - \mathbf{v}_F \cdot \mathbf{p}_s(\mathbf{r})$ (Figs. 1d and e) selectively activates delocalized quasiparticles with the Fermi velocity aligned with \mathbf{p}_s . Quasiparticle thermal transport in the low-field regime of nodal superconductors is dominated by these quasiparticles, whose density of states exhibits characteristic field dependence determined by nodal topology: $N_{\text{del}}(\varepsilon) \propto \sqrt{H}$ for line nodes and $N_{\text{del}}(\varepsilon) \propto H |\ln H|$ for point nodes [34–36]. Consequently, the thermal conductivity typically also varies as a power law of the field. Conversely, in full-gap type-II superconductors, where quasiparticles remain localized within vortex cores, while the density of states scales linearly with the number of vortices and hence the field, the thermal conductivity remains suppressed.

Critically, thermal conductivity in field sensitively probes nodal quasiparticles when \mathbf{v}_F has components parallel to both $\mathbf{p}_s(\mathbf{r})$ and \mathbf{j}_Q , but is not affected by quasiparticles with $\mathbf{v}_F \perp \mathbf{p}_s(\mathbf{r})$ or $\mathbf{v}_F \perp \mathbf{j}_Q$ (Fig. 1e). In the presence of point nodes along the b direction, applying \mathbf{H} perpendicular to the b axis ($\mathbf{H} \parallel a$ or $\mathbf{H} \parallel c$) would activate Doppler-shifted quasiparticles near the nodes due to a finite $\mathbf{p}_s \cdot \mathbf{v}_F$ component for quasiparticles with $\mathbf{v}_F \parallel \mathbf{j}_Q \parallel b$, leading to enhanced thermal conductivity. Conversely, for $\mathbf{H} \parallel b$, the supercurrent circulates in the ac -plane, resulting in $\mathbf{p}_s \cdot \mathbf{v}_F = 0$ for heat-carrying quasiparticles along the b direction; thus, κ_b would be almost insensitive to such nodes (Fig. 1d). This directional sensitivity enables spatial mapping of gap nodes on the Fermi surface. Importantly, even in full-gap superconductors with significant gap anisotropy, quasiparticles are excited at finite fields when the Doppler shift exceeds the minimum gap. Therefore, low-temperature and low-field measurements taken together yield definitive information about the gap structure.

Figures 3a–c show the temperature dependence of κ_b/T normalized by the normal-state value $(\kappa_b/T)_N$ for three field orientations down to ~ 50 mK and for the field values up to 6 T. At 0.3 K, zero-field κ_b/T exhibits strong suppression under a magnetic field of 1 T, attributed to enhanced quasiparticle scattering by magnetic flux. Given

that κ_b^{ph} is insensitive to magnetic fields, this pronounced suppression confirms the dominant quasiparticle contribution to the total thermal conductivity in the low temperature regime. This conclusion is further supported by the anisotropic field response of κ_b/T for the fields along the a and c axes, since κ_b^{ph} remains isotropic with respect to field direction normal to the heat current.

Figure 4a shows κ_b^0/T normalized by the normal-state value $(\kappa_b^0/T)_N$ under applied magnetic fields along three crystallographic directions, where $\kappa_b^0/T \equiv \lim_{T \rightarrow 0} \kappa_b(T)/T$ is obtained by polynomial extrapolation to $T \rightarrow 0$. The magnetic fields are normalized by their respective upper critical fields to account for the strong H_{c2} anisotropy: $\mu_0 H_{c2}^a = 11.7$ T, $\mu_0 H_{c2}^b = 23$ T, and $\mu_0 H_{c2}^c = 16.5$ T [37]. The thermal conductivity exhibits pronounced anisotropic field dependence at higher fields, with κ_b/T showing the weakest growth with field $\mathbf{H} \parallel b$ despite the expected normal-state contributions from vortex cores in the $\mathbf{j}_Q \parallel \mathbf{H}$ configuration. This indicates that vortex-core conduction is essentially negligible. One possible explanation for this is that the discreteness of Caroli–de Gennes–Matricon vortex core states reduces the contribution of the cores to the heat transport. Using $\Delta_0 \sim 2T_c \sim 4$ K and $\epsilon_F \sim 120$ K [12] as the characteristic superconducting gap energy scale and the Fermi energy respectively, we estimate the core level spacing to be $\Delta_0^2/\epsilon_F \sim 0.13$ K, in agreement with Ref. [38]. The phase diagram of UTe₂ for $\mathbf{H} \parallel b$ is complex at high fields, with re-entrant superconductivity and other phases. However, in the range where the measurements are done the field in the vortex core is still far below H_{c2} , and therefore emergence of additional order parameters, while possible, does not seem likely.

The low-field results provide strong evidence for pseudo-point nodes, characterized by gap minima that remain finite rather than reaching zero. The in-plane field response of κ_b^0/T shown in Fig. 4b offers critical insights into the detailed structure of the superconducting gap. The most notable feature is the apparent kink at a threshold field $H_a^*/H_{c2}^a \sim 0.015$ (arrow) in the field dependence of κ_b^0/T for $\mathbf{H} \parallel a$ for both samples #A

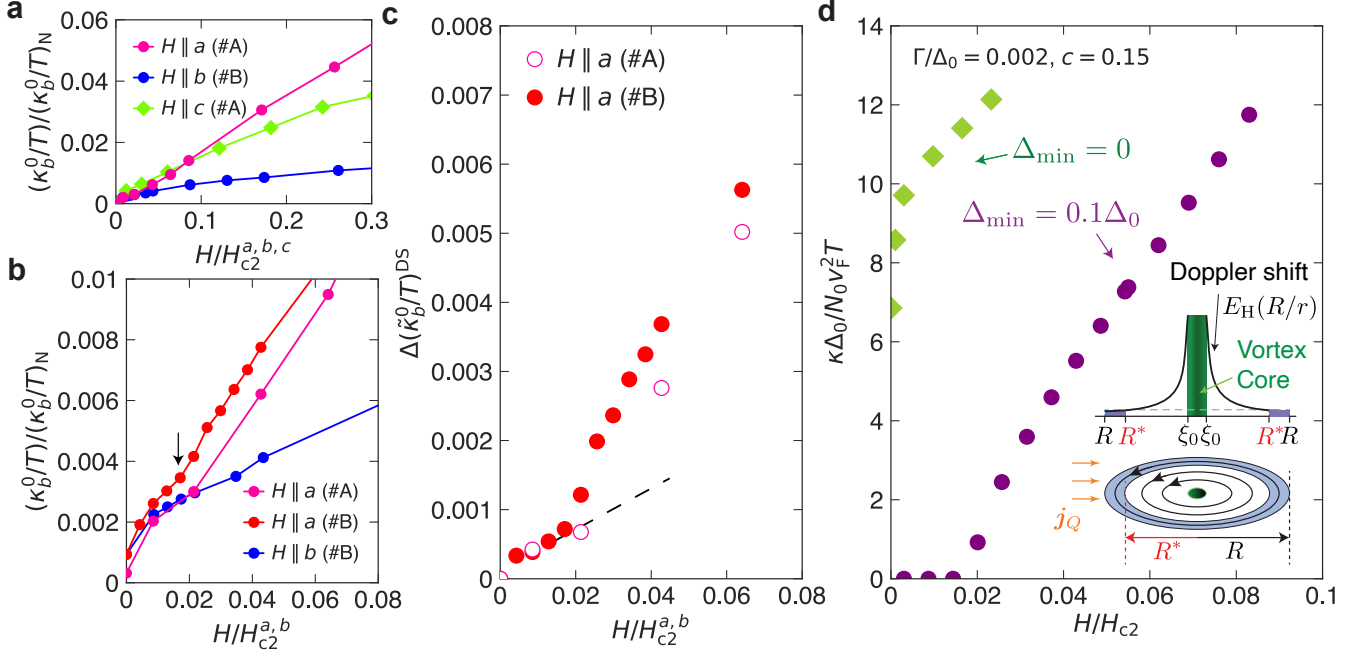


FIG. 4. **Field-enhanced thermal conductivity in the $T \rightarrow 0$ limit:** **a–c**, The zero-temperature limit of the b -axis thermal conductivity divided by temperature κ_b^0/T , normalized by the normal state value $(\kappa_b^0/T)_N$, plotted as a function of magnetic field applied parallel to the a , b , and c axes. The magnetic fields are normalized by the corresponding upper critical field $H_{c2}^{a,b,c}$. **a**, $(\kappa_b^0/T)/(\kappa_b^0/T)_N$ as a function of $H/H_{c2}^{a,b,c}$ for $\mathbf{H} \parallel a$, b and c . **b**, $(\kappa_b^0/T)/(\kappa_b^0/T)_N$ as a function of $H/H_{c2}^{a,b}$ for $\mathbf{H} \parallel a$ and b . For $\mathbf{H} \parallel a$, a kink is observed at $H^*/H_{c2}^a \approx 0.015$ (arrow), below which $(\kappa_b^0/T)/(\kappa_b^0/T)_N$ exhibits nearly isotropic behavior, whereas pronounced anisotropy develops above this characteristic threshold field. **c**, The red circles show the thermal conductivity difference $\Delta(\tilde{\kappa}_b^0/T)^{\text{DS}} = [\Delta(\kappa_b^0/T)/(\kappa_b^0/T)_N]_{\mathbf{H} \parallel a} - [\Delta(\kappa_b^0/T)/(\kappa_b^0/T)_N]_{\mathbf{H} \parallel b}$ for $\#B$, which represents the difference between field configurations with and without the Doppler shift contribution. For comparison, pink open circles represent the corresponding difference calculated by subtracting the $\#B$ ($\mathbf{H} \parallel b$) data from the $\#A$ ($\mathbf{H} \parallel a$) data. Both datasets exhibit good agreement. The dashed line is a guide to the eye. **d**, Magnetic field dependence of the residual thermal conductivity term for the true point nodes ($\Delta_{\min} = 0$) and pseudo-nodes ($\Delta_{\min} = 0.1\Delta_0$) in a model of a Fermi surface with a square cross-section in the a - b plane and nodes/minima along the b axis, as described in the Supplementary Information. Inset: Schematic of Doppler shift effects in a model circular unit cell of the vortex lattice (radius R). Below the threshold field $E_H^* = \Delta_{\min}$ the Doppler shift at distances $R > r > R^* \sim RE_H/\Delta_{\min}$ is insufficient to generate unpaired quasiparticles (blue ring). For the heat current normal to the field this yields an effective thermally insulating barrier, preventing net heat conduction, see text for details.

and $\#B$. This kink at the threshold is more clearly observed in Fig. 4c showing the difference between $\mathbf{H} \parallel \mathbf{j}_Q$ ($\mathbf{H} \parallel b$) and $\mathbf{H} \perp \mathbf{j}_Q$ ($\mathbf{H} \parallel a$) configurations. These results demonstrate that quasiparticle excitations undergo a qualitative change at this threshold field. Below H_a^* , κ_b^0/T exhibits only weak anisotropy between field orientations. Above H_a^* , the in-plane response becomes strongly anisotropic, with $\mathbf{H} \perp \mathbf{j}_Q$ yielding substantially larger values than $\mathbf{H} \parallel \mathbf{j}_Q$. The perpendicular field geometry more efficiently generates Doppler-shifted quasiparticles with velocities aligned along the thermal gradient. Consequently, the absence of significant anisotropy below H_a^* indicates that such Doppler-shifted quasiparticles contribute very little to thermal transport across the vortex lattice. This is consistent with a finite minimal gap.

Consider the geometry for fields normal to the heat current, as illustrated in Fig. 4d. In the approximation where the vortex unit cell is a circle of radius $R \sim \xi_0 \sqrt{H_{c2}/H}$ (ξ_0 is the coherence length), the characteris-

tic Doppler shift energy scale $E_H = a\Delta_0 \sqrt{H/H_{c2}}$, with $a \sim 1$ is the *minimal* Doppler shift at the edge of the unit cell. The Doppler shift itself varies as $E_H(R/r)$ with the distance r to the vortex core inside the unit cell. In the calculations below we took $a = 0.72$, which is the value accepted in Ref. [30], but the qualitative picture does not depend on the exact value of a . To generate the unpaired quasiparticles in the absence of impurities, the Doppler shift needs to exceed the gap amplitude. Therefore in the presence of the minimal gap, such quasiparticles are generated everywhere in real space above the threshold field, $E_H^* = \Delta_{\min}$, or $H^*/H_{c2} = a^{-2}(\Delta_{\min}/\Delta_0)^2$. Below this field the unpaired quasiparticles only appear inside the circle of a radius $R^* = R(E_H/\Delta_{\min}) < R$, while at $R^* < r < R$ the system is fully gapped (see Fig. 4d).

Heat current normal to the vortices samples regions with all the Doppler shifts, and therefore the thermally insulating fully gapped region prevents heat conduction below H^* , yielding a sharp onset once this field is exceeded. This is shown in the main panel of Fig. 4d,

where we calculated the thermal conductivity following Ref. [39], which took the “series” resistor connection to model transport normal to the vortices. The threshold field is clearly seen at $H/H_{c2} \sim 0.015$ for the pseudonodal model assuming $\Delta_{\min} = 0.1\Delta_0$ and is absent for true nodes. Very rapid rise of the thermal conductivity at low fields for $\Delta_{\min} = 0$ is due to the square shape of the Fermi surface assumed in the model, see Supplementary Information for details. Therefore in this model the experimental results are consistent with $\Delta_{\min} = 0.1\Delta_0$ (Supplementary Fig. 5), although the exact magnitude of the minimal gap depends on the choice of parameter a . In our model, as in Ref. [39], the quasiparticles sample all available Doppler shift values along their path. We expect that beyond the semiclassical approach there will be finite, albeit small, heat transport across the classically forbidden regions, but expect that the kink at the threshold field will remain.

Notably, the experimentally measured κ/T exhibits a slight increase with applied field even below the threshold, in contrast to theoretical predictions. The discrepancy reflects limitations of the Doppler shift picture for transport. In the Doppler shift method one computes the local value of the transport coefficient. However, if the range over which the corresponding correlation function decays encompasses regions of different superfluid velocities, the results are only qualitatively correct even at low fields. In particular, if the mean free path is comparable to or greater than the width of the “forbidden” region in the schematic of Fig. 4d, the quasiparticles can traverse that region, and the heat current will be finite, albeit reduced.

Quantum oscillation studies, which serve as a bulk probe of electronic structure, have demonstrated that UTe_2 possesses distinct cylindrical electron and hole Fermi surface sheets that are topologically separated, with no connectivity at Brillouin zone boundaries [40]. Initially, quantum oscillation measurements suggested the presence of a 3D Fermi surface pocket [41]. However, subsequent high-resolution studies found no evidence for 3D Fermi surface sections [12] and demonstrated that the oscillations originate from quantum interference effects between quasi-2D sheets [42, 43]. Based on these findings, we adopt a quasi-2D Fermi surface topology. In this topology, the gap function is nodeless due to the absence of Fermi surface sections extending along the c -axis direction, and the thermal conductivity under elevated fields reveals intrinsic gap anisotropy in 2D Fermi sheets.

Based on the observed fully gapped superconducting behavior in the ab -plane, the order parameter is expected to belong to either the A_u or B_{1u} irreducible representation. In the B_{1u} state, the gap function exhibits point nodes along the c axis; however, these remain experimentally inaccessible owing to the absence of Fermi surface sections along this direction. Within the quasi-2D electronic structure, theoretical calculations suggest that UTe_2 likely realizes a topological crystalline superconducting state protected by time-reversal and crystal

symmetries [44]. Both pairing states support Majorana edge modes at the same open boundaries perpendicular to the a or b axes. The distinction lies in their dispersion: a flat band for the B_{1u} state and a linearly dispersing mode for the A_u state. These theoretical predictions could be tested by orientation-resolved STM, although surface CDW effects may obscure intrinsic topological superconducting signatures.

We next compare our conclusions to the reported results from bulk probes of the gap function, such as nuclear magnetic resonance (NMR) and specific heat measurements. The observed suppression of NMR Knight shifts along all crystallographic axes appears consistent with A_u symmetry [45]; however, this holds only when the \mathbf{d} -vector contains linear momentum terms proportional to k_i (where $i = a, b, c$). However, \mathbf{d} -vectors incorporating higher-order momentum components, such as cubic terms $k_a k_b k_c$, produce finite contributions along all crystallographic directions, resulting in Knight shift suppression along all axes irrespective of the underlying gap symmetry. Consequently, the observed Knight shift suppression cannot unambiguously distinguish between A_u , B_{1u} , B_{2u} , and B_{3u} representations, nor can it conclusively identify the fully gapped superconducting order.

Specific-heat measurements on UTe_2 exhibit power-law behavior, $C_{el} \propto T^n$ with $n \approx 3$ in zero field, attributed to quasiparticle excitations from point nodes [46, 47]. The anisotropic field dependence of C_{el} has been interpreted as evidence for point nodes oriented along the b -axis [47]. However, the proposed b -axis pseudo point node scenario consistently explains both behaviors (Supplementary Fig. 6). The gap minima revealed by thermal conductivity measurements remain inaccessible to specific-heat measurements due to Schottky anomalies below $T \sim 0.3$ K, which are strongly enhanced under applied magnetic fields. As shown in the Supplementary Information, the T -dependence of the specific heat exhibits $C/T \propto T^2$ dependence above 0.3 K for pseudo point nodes with $\Delta_{\min}/\Delta_0 \approx 0.1$. Magnetic field dependence of the specific heat is also unlikely to identify a small residual gap. While for the point nodes the expected field behavior is $C/T \propto -(H/H_{c2}) \ln H/H_{c2}$, for a small gap it becomes $C/T \propto -(H/H_{c2}) \ln [H/H_{c2} + (\Delta_{\min}/a\Delta_0)^2]$, and hence the substantial difference is only observed for $H \ll H^*$, where such measurements are not possible.

Finally, the emergence of a strongly anisotropic superconducting gap exhibiting pseudo point nodes in UTe_2 is highly unusual and represents a remarkable example of unconventional superconductivity. A possible mechanism may involve an accidental gap minimum arising from specific band structure characteristics. However, the formation of a pseudo point nodal gap characterized by a finite gap anisotropy ratio $\Delta_{\min}/\Delta_0 \sim 0.1$ would necessitate precise fine-tuning of both the pairing interaction strength and the degree of Fermi surface corrugation. Nevertheless, both the electron and hole Fermi surfaces are rather smooth, without any local corrugation that could produce point nodes [12]. Therefore, the

Fermi surface geometry and topology of UTe_2 are relatively straightforward, and the accidental emergence of such an unconventional gap structure, while perhaps not theoretically precluded entirely, appears highly improbable. This suggests that the pseudo point node represents an anomalous behavior from the perspective of conventional pairing mechanisms.

The presence of pseudo-point nodes in UTe_2 imposes important constraints on the superconducting gap function and its formation mechanism. Non-unitary mixing states with broken time-reversal symmetry cannot readily explain this phenomenon. Indeed, non-unitary mixing of B_{2u} symmetry, which has point nodes along the b -axis, with a small admixture of other symmetries (e.g., $B_{2u} + i\alpha A_u$ with $\alpha \ll 1$) merely shifts the node positions while preserving the nodes. To completely lift the point nodes, it is necessary to consider unitary mixing states where two order parameter components, such as $B_{2u} + \alpha A_u$, possess real relative phases. Alternatively, pseudo-point nodes can be interpreted as nodal structures that are quasi-protected by crystal symmetry but partially lifted by weak symmetry-breaking perturbations, possibly arising from spin-orbit coupling or weak interorbital hybridization. This results in the formation of a highly anisotropic superconducting gap with pronounced minima along specific crystallographic directions in momentum space. Further theoretical analysis and experimental verification are required to identify the dominant mechanism underlying pseudo-point node formation in UTe_2 .

METHODS

High-quality single-crystal samples of UTe_2 were grown by the molten-salt method. Both crystals were cut to dimensions suitable for thermal-conductivity measurements, typically with length $\sim 360 \mu\text{m}$ ($\parallel b$), width

$\sim 370 \mu\text{m}$ ($\parallel a$), and thickness $\sim 110 \mu\text{m}$ ($\parallel c$). Thermal conductivity was measured using the standard steady-state method with one heater and two thermometers, applying a temperature gradient along the b axis. The typical thermal gradient was less than 3% of the bath temperature. To ensure good electrical and thermal contacts, four platinum wires were attached by spot welding. Electrical resistivity was measured *in situ* within the same set-up used for thermal-conductivity measurements.

ACKNOWLEDGMENTS

We thank D. Aoki, A. Balatsky, S. Fujimoto, H. Kon-tani, S. Lin, T. Shibauchi, S. Suetsugu, J. Thompson, and Y. Yanase for insightful discussions. Work at the Los Alamos National Laboratory was supported by the U.S. Department of Energy, Office of Basic Energy Sciences, Division of Materials Science and Engineering project “Quantum Fluctuations in Narrow-band Systems”. S.H. acknowledges the Director’s Postdoctoral Fellowship through the Laboratory Directed Research and Development Program at Los Alamos National Laboratory.

AUTHOR CONTRIBUTIONS

S.H. and Y.M. conceived the study. M.M.B., E.D.B and P.F.S.R. synthesized the samples. S.H., K.I., and R.M. performed thermal conductivity and resistivity measurements. S.H. analyzed the data, and I.V. performed theoretical calculations. All authors discussed the results. S.H., Y.M. and I.V. prepared the manuscript with input from all authors.

-
- [1] Nayak, C., Simon, S. H., Stern, A., Freedman, M. & Das Sarma, S. Non-Abelian anyons and topological quantum computation. *Rev. Mod. Phys.* **80**, 1083–1159 (2008).
 - [2] Ran, S. *et al.* Nearly ferromagnetic spin-triplet superconductivity. *Science* **365**, 684–687 (2019).
 - [3] Aoki, D. *et al.* Unconventional superconductivity in UTe_2 . *J. Phys. Condens. Matter* **34**, 243002 (2022).
 - [4] Ran, S. *et al.* Extreme magnetic field-boosted superconductivity. *Nat. Phys.* **15**, 1250–1254 (2019).
 - [5] Knafo, W. *et al.* Comparison of two superconducting phases induced by a magnetic field in UTe_2 . *Commun. Phys.* **4**, 40 (2021).
 - [6] Wu, Z. *et al.* A quantum critical line bounds the high field metamagnetic transition surface in UTe_2 . *Phys. Rev. X* **15**, 021019 (2025).
 - [7] Braithwaite, D. *et al.* Multiple superconducting phases in a nearly ferromagnetic system. *Commun. Phys.* **2**, 147 (2019).
 - [8] Thomas, S. *et al.* Evidence for a pressure-induced antiferromagnetic quantum critical point in intermediate-valence UTe_2 . *Sci. Adv.* **6**, eabc8709 (2020).
 - [9] Saxena, S. *et al.* Superconductivity on the border of itinerant-electron ferromagnetism in UGe_2 . *Nature* **406**, 587–592 (2000).
 - [10] Aoki, D. *et al.* Coexistence of superconductivity and ferromagnetism in URhGe . *Nature* **413**, 613–616 (2001).
 - [11] Huy, N. T. *et al.* Superconductivity on the Border of Weak Itinerant Ferromagnetism in UCoGe . *Phys. Rev. Lett.* **99**, 067006 (2007).
 - [12] Eaton, A. *et al.* Quasi-2D Fermi surface in the anomalous superconductor UTe_2 . *Nat. Commun.* **15**, 223 (2024).
 - [13] Ishizuka, J., Sumita, S., Daido, A. & Yanase, Y. Insulator-Metal Transition and Topological Superconductivity in UTe_2 from a First-Principles Calculation. *Phys. Rev. Lett.* **123**, 217001 (2019).

- [14] Xu, Y., Sheng, Y. & Yang, Y.-f. Quasi-two-dimensional Fermi surfaces and unitary spin-triplet pairing in the heavy fermion superconductor UTe_2 . *Phys. Rev. Lett.* **123**, 217002 (2019).
- [15] Aishwarya, A. *et al.* Magnetic-field-sensitive charge density waves in the superconductor UTe_2 . *Nature* **618**, 928–933 (2023).
- [16] Talavera, P. G. *et al.* Surface charge density wave in UTe_2 . *arXiv:2504.12505* (2025).
- [17] Kengle, C. S. *et al.* Absence of bulk charge density wave order in the normal state of UTe_2 . *Nat. Commun.* **15**, 9713 (2024).
- [18] Gu, Q. *et al.* Pair wave function symmetry in UTe_2 from zero-energy surface state visualization. *Science* **388**, 938–944 (2025).
- [19] Li, Z. *et al.* Observation of odd-parity superconductivity in UTe_2 . *Proc. Natl. Acad. Sci. USA* **122**, e2419734122 (2025).
- [20] Yoon, H. *et al.* Probing p-wave superconductivity in UTe_2 via point-contact junctions. *npj Quantum Mater.* **9**, 91 (2024).
- [21] Ishihara, K. *et al.* Chiral superconductivity in UTe_2 probed by anisotropic low-energy excitations. *Nat. Commun.* **14**, 2966 (2023).
- [22] Bae, S. *et al.* Anomalous normal fluid response in a chiral superconductor UTe_2 . *Nat. Commun.* **12**, 1–5 (2021).
- [23] Iguchi, Y. *et al.* Microscopic Imaging Homogeneous and Single Phase Superfluid Density in UTe_2 . *Phys. Rev. Lett.* **130**, 196003 (2023).
- [24] Girod, C. *et al.* Thermodynamic and electrical transport properties of UTe_2 under uniaxial stress. *Phys. Rev. B* **106**, L121101 (2022).
- [25] Theuss, F. *et al.* Single-component superconductivity in UTe_2 at ambient pressure. *Nature Physics* **20**, 1124–1130 (2024).
- [26] Ajeesh, M. *et al.* Fate of time-reversal symmetry breaking in UTe_2 . *Phys. Rev. X* **13**, 041019 (2023).
- [27] Azari, N. *et al.* Absence of spontaneous magnetic fields due to time-reversal symmetry breaking in bulk superconducting UTe_2 . *Phys. Rev. Lett.* **131**, 226504 (2023).
- [28] Matsuda, Y., Izawa, K. & Vekhter, I. Nodal structure of unconventional superconductors probed by angle resolved thermaltransport measurements. *J. Phys. Condens. Matter* **18**, R705 (2006).
- [29] Suetsugu, S. *et al.* Fully gapped pairing state in spin-triplet superconductor UTe_2 . *Sci. Adv.* **10**, eadk3772 (2024).
- [30] Hayes, I. M. *et al.* Robust nodal behavior in the thermal conductivity of superconducting UTe_2 . *Phys. Rev. X* **15**, 021029 (2025).
- [31] Sakai, H. *et al.* Single crystal growth of superconducting UTe_2 by molten salt flux method. *Phys. Rev. Mater.* **6**, 073401 (2022).
- [32] Hirschfeld, P. J., Wölfle, P. & Einzel, D. Consequences of resonant impurity scattering in anisotropic superconductors: Thermal and spin relaxation properties. *Phys. Rev. B* **37**, 83–97 (1988).
- [33] Mishra, V., Wang, G. & Hirschfeld, P. Thermal conductivity of nonunitary triplet superconductors: application to UTe_2 . *Front. Phys.* **12**, 1397524 (2024).
- [34] Graf, M. J., Yip, S., Sauls, J. & Rainer, D. Electronic thermal conductivity and the Wiedemann-Franz law for unconventional superconductors. *Phys. Rev. B* **53**, 15147 (1996).
- [35] Vekhter, I. & Houghton, A. Quasiparticle thermal conductivity in the vortex state of high- T_c cuprates. *Phys. Rev. Lett.* **83**, 4626 (1999).
- [36] Adachi, H., Miranovic, P., Ichioka, M. & Machida, K. Quasi-classical calculation of the mixed-state thermal conductivity in *s*- and *d*-wave superconductors. *J. Phys. Soc. Jpn.* **76**, 064708–064708 (2007).
- [37] Wu, Z. *et al.* Enhanced triplet superconductivity in next-generation ultraclean UTe_2 . *Proc. Natl. Acad. Sci. USA* **121**, e2403067121 (2024).
- [38] Sharma, N. *et al.* Observation of Persistent Zero Modes and Superconducting Vortex Doublets in UTe_2 . *ACS Nano* **19**, 31539–31550 (2025).
- [39] Kübert, C. & Hirschfeld, P. J. Quasiparticle Transport Properties of *d*-Wave Superconductors in the Vortex State. *Phys. Rev. Lett.* **80**, 4963–4966 (1998).
- [40] Aoki, D. *et al.* de Haas–van Alphen Oscillations for the Field Along *c*-axis in UTe_2 . *J. Phys. Soc. Jpn.* **92**, 065002 (2023).
- [41] Broyles, C. *et al.* Revealing a 3D Fermi surface pocket and electron-hole tunneling in UTe_2 with quantum oscillations. *Phys. Rev. Lett.* **131**, 036501 (2023).
- [42] Weinberger, T. *et al.* Quantum interference between quasi-2D Fermi surface sheets in UTe_2 . *Phys. Rev. Lett.* **132**, 266503 (2024).
- [43] Husstedt, F. *et al.* Slow magnetic quantum oscillations in the *c*-axis magnetoresistance of UTe_2 . *Phys. Rev. B* **111**, 235131 (2025).
- [44] Tei, J., Mizushima, T. & Fujimoto, S. Possible realization of topological crystalline superconductivity with time-reversal symmetry in UTe_2 . *Phys. Rev. B* **107**, 144517 (2023).
- [45] Matsumura, H. *et al.* Large Reduction in the *a*-axis Knight Shift on UTe_2 with $T_c = 2.1$ K. *J. Phys. Soc. Jpn.* **92**, 063701 (2023).
- [46] Metz, T. *et al.* Point-node gap structure of the spin-triplet superconductor UTe_2 . *Phys. Rev. B* **100**, 220504 (2019).
- [47] Lee, S. *et al.* Anisotropic field-induced changes in the superconducting order parameter of UTe_2 . *Phys. Rev. Research* **7**, L022053 (2025).